Measurements of fundamental properties of homogeneous tissue phantoms

Maciej S. Wróbel
Alexey P. Popov
Alexander V. Bykov
Matti Kinnunen
Malgorzata Jędrzejewska-Szczerska
Valery V. Tuchin

SPIE.

Measurements of fundamental properties of homogeneous tissue phantoms

Maciej S. Wróbel,[a,*] Alexey P. Popov,[b] Alexander V. Bykov,[b] Matti Kinnunen,[b] Malgorzata Jędrzejewska-Szczerska,[a] and Valery V. Tuchin[b,c,d]
[a]Gdańsk University of Technology, Faculty of Electronics, Telecommunications and Informatics, Department of Metrology and Optoelectronics, Gabriela Narutowicza Street 11/12, 80-233 Gdańsk, Poland
[b]University of Oulu, Faculty of Information Technology and Electrical Engineering, Optoelectronics and Measurement Techniques Laboratory, P.O. Box 4500, Oulu 90014, Finland
[c]Saratov State University, Research-Educational Institute of Optics and Biophotonics, Saratov 410012, Russia
[d]Institute of Precise Mechanics and Control of Russian Academy of Sciences, Saratov 410028, Russia

Abstract. We present the optical measurement techniques used in human skin phantom studies. Their accuracy and the sources of errors in microscopic parameters' estimation of the produced phantoms are described. We have produced optical phantoms for the purpose of simulating human skin tissue at the wavelength of 930 nm. Optical coherence tomography was used to measure the thickness and surface roughness and to detect the internal inhomogeneities. A more detailed study of phantom surface roughness was carried out with the optical profilometer. Reflectance, transmittance, and collimated transmittance of phantoms were measured using an integrating-sphere spectrometer setup. The scattering and absorption coefficients were calculated with the inverse adding-doubling method. The reduced scattering coefficient at 930 nm was found to be $1.57 \pm 0.14~\text{mm}^{-1}$ and the absorption was $0.22 \pm 0.03~\text{mm}^{-1}$. The retrieved optical properties of phantoms are in agreement with the data found in the literature for real human tissues. © *The Authors. Published by SPIE under a Creative Commons Attribution 3.0 Unported License. Distribution or reproduction of this work in whole or in part requires full attribution of the original publication, including its DOI.* [DOI: 10.1117/1.JBO.20.4.045004]

1 Introduction

The emergence of new optical measurement techniques in the field of biophotonics has increased the interest in the possibility of their use for medically relevant, noninvasive *in vivo* imaging and measurements.[1–10] The development and evaluation of such methods require frequent calibration of the devices. However, real biological tissues differ greatly from each other and their optical properties are susceptible to rapid changes over time and with varying environmental conditions.[11–14] This calls for the development of substitutes of specific biological tissues, which are optical tissue-mimicking phantoms.[15–18] One type of phantom is composed of solid flexible materials with added scattering and absorbing particles suspended in a transparent matrix material. To assure phantoms as a valid and reliable standard for noninvasive optical diagnostic techniques,[16–20] their optical properties must be precisely measured and controlled by the fabrication process.[21–26]

The scattering, absorption, and scattering anisotropy are the fundamental microscopic properties that describe the photon migration in a turbid medium, such as tissues;[27,28] thus, the design and production processes of tissue phantoms focus on their exact matching. These microscopic properties can be measured indirectly by measuring macroscopic parameters, such as reflectance or transmittance, and by applying a model of light propagation.[29] The inverse adding-doubling (IAD) method can be used to calculate the coefficients of the sample from reflectance, transmittance, and collimated transmittance measurements.[30,31] This method relies on the iterative solving of the radiative transport equation with the adding-doubling method and yields the absorption and scattering coefficients, as well as the anisotropy factor. The sample is assumed to be an infinite plane-parallel slab with known thickness and refractive index (RI). The optical properties of the sample are assumed to be uniform. IAD has been proven to provide results relatively quickly with a relative error of 2% to 3%. It has been reported that the errors in retrieval of the optical properties of a material are roughly one level of magnitude larger, due to measurements, than the method itself.[31] Therefore, proper measurements are of the utmost importance due to their use as input parameters in the IAD method.

The purpose of this paper is the production and characterization of a series of phantoms with different thicknesses as valid substitutes for biological samples (human skin) for noninvasive diagnostic methods, with their potential use in medicine. We present a variety of optical measurement techniques, which were used for reconstruction of the most important properties of phantoms. Measured parameters include the optical properties, geometry, and surface roughness.

2 Phantom Fabrication Process

Phantoms used in this study mimic human skin at the central wavelength of 930 nm, common for optical coherence tomography (OCT) devices. The scattering properties were modeled on the basis of the Mie theory and known optical properties of the constituent materials.[32–35] One series of scattering and nonabsorbing phantoms with variable thickness from 200 μm

---

*Address all correspondence to: Maciej S. Wróbel, E-mail: maciejswrobel@gmail.com

up to 2 mm was produced. Additional absorption was introduced to the second series of phantoms with the same scattering and thickness as the previous series. The phantoms were made using zinc oxide (ZnO) nanoparticles as a scattering agent, the matrix material, and an absorbing substance. A polyvinyl chloride-plastisol (PVCP) two-component stock solution (M-F Manufacturing Co., Fort Worth, Texas) was used as a matrix material for the phantom fabrication. PVCP has a RI of 1.44 (at 930 nm) and becomes transparent due to polymerization after curing at a high temperature. The desired scattering was obtained using ZnO nanoparticles powder (Sigma-Aldrich, Germany) with an average size of 340 nm. PVCP solution was thoroughly mixed with ZnO to ensure homogenous distribution. For the absorbing phantoms, a 0.1% [v/v] amount of ink was added to the mixture. The mixture was sonicated for 15 min to destroy particle clusters and to evenly distribute the particles in the suspension. It was then poured into plane rectangular molds with different thicknesses and degassed to remove trapped air bubbles. The phantoms solidified after heating at 180°C for 1 h.

3 Fundamental Parameters of Tissue Phantoms

The absorption coefficient μ_a describes the attenuation of light due to absorption by the medium at a certain wavelength. This parameter of skin phantoms depends on concentration of absorbers in skin, mainly melanin and hemoglobin. The reduced scattering coefficient μ_s' describes the photon migration process in tissues in the diffuse regime.[16] The anisotropy factor g (a mean cosine of the scattering angle) allows for calculation of the scattering coefficient μ_s, according to the equation:

$$\mu_s = \frac{\mu_s'}{1-g}, \qquad (1)$$

which fully describes the scattering properties of the material.[27–31] To estimate the value of μ_s, it is necessary to measure the transmittance of the collimated light from the investigated samples. Precise matching of these parameters of phantoms and biotissues is crucial for producing reliable phantoms. The optical signal response of a phantom is then identical to that of a tissue making it valid for instrument calibration.[7–9,36–39] Therefore, the exact reconstruction of the scattering and absorption may be performed based only on accurate measurements. We estimated the coefficients μ_a, μ_s', and g for each phantom using spectrometric measurements and the IAD calculations. The algorithm for retrieval of optical properties is shown in Fig. 1.

3.1 Spectrometric Measurements

Measurements of total transmittance, total reflectance, and collimated transmittance of the phantoms in the wavelength range of 400 to 1100 nm were performed using an OL-750 spectrophotometer system with integrating spheres (Optronic Laboratories, USA). Diffusely reflected light was collected in an OL 740-70 integrating sphere diffuse reflectance attachment and transmittance of the samples was measured in OL IS-670-LED integrating sphere. Both reflectance and transmittance integrating spheres are 6-in. in diameter with internal PTFE coating yielding >99% reflectivity in the 300- to 1700-nm wavelength range. The sample measurement area was 3 mm in diameter in both cases. Collimated transmittance was measured using OL 740-73Q quartz lens transmission attachment.
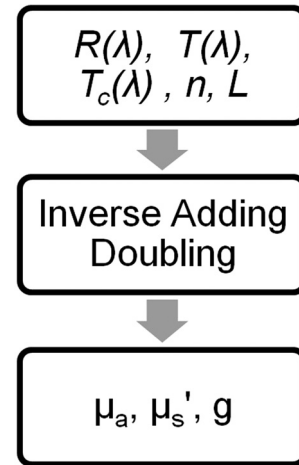

Fig. 1 Algorithm for the determination of fundamental parameters of phantoms: first, the reflectance $R(\lambda)$, transmittance $T(\lambda)$, collimated transmittance $T_c(\lambda)$, refractive index n, and phantom thickness L are measured. Then, inverse adding-doubling (IAD) is used to calculate the absorption coefficient μ_a, reduced scattering coefficient μ_s', and anisotropy factor g from the measurement results by iteratively solving the radiative transfer equation.

Total reflectance $R(\lambda)$, transmittance $T(\lambda)$, and collimated transmittance $T_c(\lambda)$ spectra were measured by the means of spectrophotometry. These are the most important measurements used for determination of phantoms' properties.

Total reflectance $R(\lambda)$ spectra were obtained using the comparison method.[30] Two calibration measurements were recorded, one with the beam focused on the comparison sample (sphere wall) and other with the beam focused on a standard reference sample. Thus, the integrating sphere calibration factor $C(\lambda)$ is obtained for each wavelength:

$$C(\lambda) = \frac{R_S(\lambda)S_{CS}(\lambda)}{S_{SR}(\lambda)}, \qquad (2)$$

where $R_S(\lambda)$ is the reflectance of the standard reflectance sample, $S_{CS}(\lambda)$ is the spectrum with the beam focused on the comparison sample, and $S_{SR}(\lambda)$ is the spectrum with the beam focused on the standard reflectance sample. Then the test samples are measured the same way as the calibration scans but with the substitution of a standard reference sample with a test sample. Using the sphere calibration factor, the reflectance of the sample can be calculated as follows:

$$R(\lambda) = \frac{C(\lambda)S_T(\lambda)}{S_{CT}(\lambda)}, \qquad (3)$$

where $R(\lambda)$ is the reflectance of the test sample, $S_T(\lambda)$ is the spectrum with the beam focused on the test sample, and $S_{CT}(\lambda)$ is the spectrum with the beam focused on the comparison sample. The spectra were obtained at several spots in the center of the phantom area and averaged. The integration time was 4 s with multiple averages. The results are depicted in Fig. 2.

For the nonabsorbing phantoms, reflectance greatly depends on their thickness. Even small sample-to-sample variations in thickness (about 15 μm, see Sec. 3.3) are noticeable in the reflectance measurements. In the case of absorbing phantoms, the reflectance of the phantoms thicker than 200 μm is roughly the same regardless of their thickness and is significantly lower
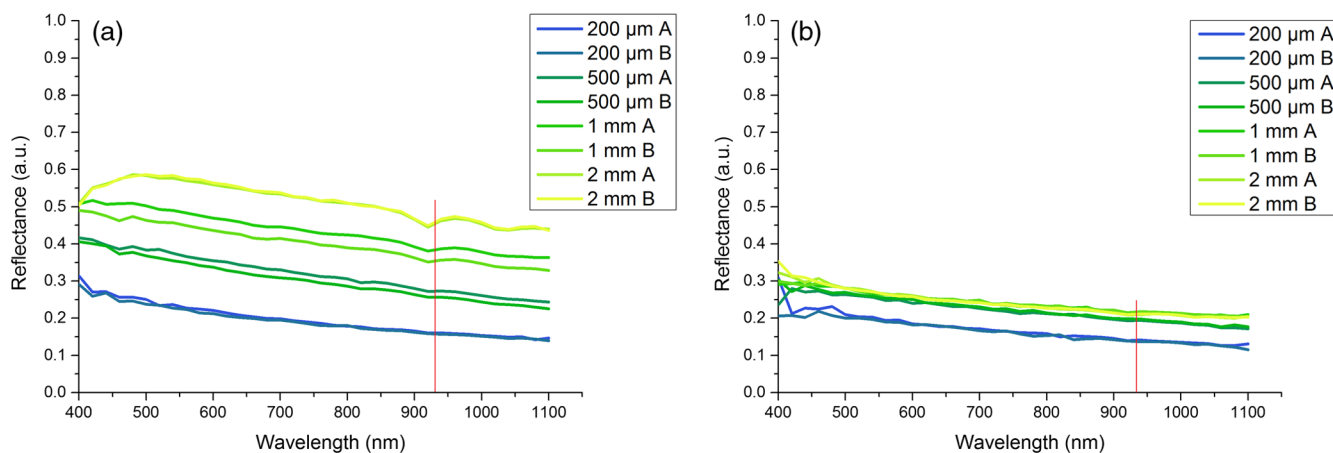
Fig. 2 Total reflectance versus wavelength for phantoms (a) without absorbing centers and (b) with absorbing centers for different phantom thicknesses. A and B denote the phantom production series. Reflectance heavily depends on the thickness of the phantom. Additional absorption further reduces the reflectance to such extent that the phantoms thicker than 200 μm have roughly identical reflectance. Vertical line indicates 930-nm wavelength, for which the phantoms were modeled.

than in case of the nonabsorbing phantoms. The intensity of the backscattered light drops significantly with penetration depth. After a certain depth, all light is absorbed and no more is backscattered, regardless of the material thickness. Reflectance slightly decreases with the wavelength in both cases.

The total transmittance of the sample $T(\lambda)$ was calculated as follows:

$$T(\lambda) = T_S(\lambda)/T_{cal}(\lambda), \tag{4}$$

where $T_S(\lambda)$ is the spectrum measured with a sample, and $T_{cal}(\lambda)$ is the instrument calibration spectrum. The spectra were measured at several spots and averaged the same way as for reflectance measurements.

Total transmittance increases with the wavelength and is inversely proportional to the reflectance (Fig. 3). It heavily depends on the phantom thickness. With the introduction of absorption, transmittance drops by the same factor for each thickness. Similar to the reflectance measurements, small variations in the thickness of the phantoms are noticeable in the transmittance spectra. The measured transmission dependence on thickness and absorption complies with theoretical prediction.

The collimated transmittance $T_c(\lambda)$ (or unscattered transmittance) was measured using a collimator with a 1.5-mm diameter pinhole and was calculated similar to transmittance:

$$T_c(\lambda) = T_S(\lambda)/T_{cal}(\lambda), \tag{5}$$

where $T_S(\lambda)$ is the spectrum measured with a sample and $T_{cal}(\lambda)$ is the instrument calibration spectrum. Also in this case, the measurements were performed over several spots on the phantom surface but the integration time was increased to 8 s as well as the number of averages due to the very low amount of light reaching the detector.

Collimated transmittance measurements are the most susceptible to errors due to low amounts of light and, consequently, a poor signal-to-noise ratio, yielding the least accurate data. The collimated transmittance values increase with the wavelength as well as with the phantom thickness decrease (Fig. 4). Small variations in thickness are very pronounced and vary significantly depending on the measured surface area. The introduction of absorbers reduces the transmittance of all phantoms.
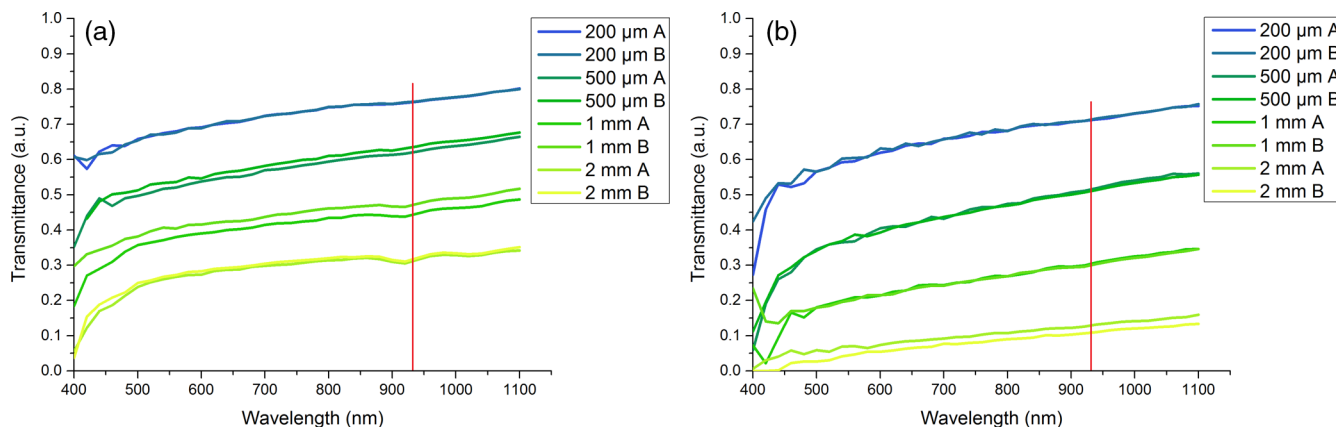

Fig. 3 Total transmittance versus wavelength for phantoms (a) without absorbing centers and (b) with absorbing centers for different phantom thicknesses. A and B denote the phantom production series. Vertical line indicates 930-nm wavelength, for which the phantoms were modeled.
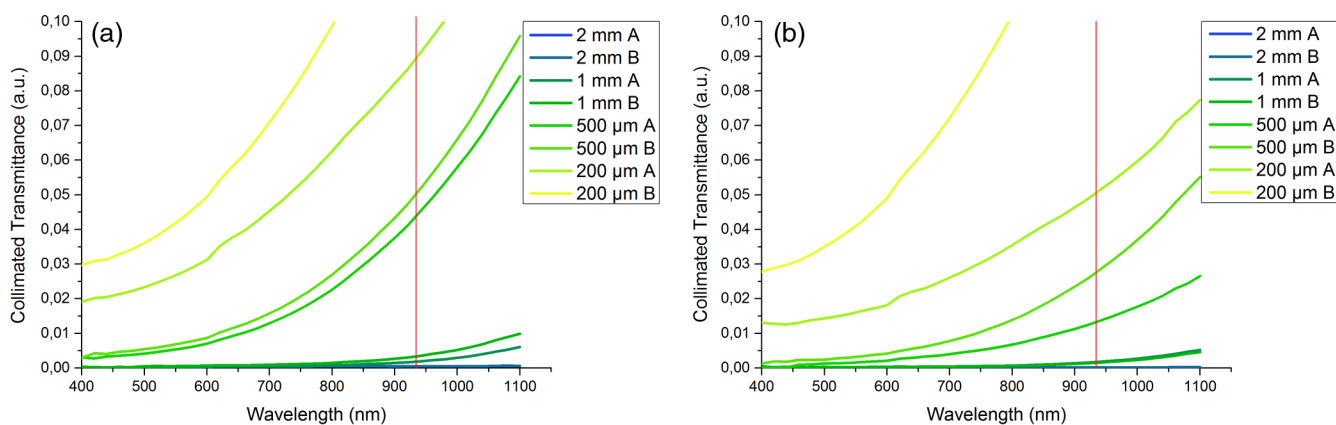
Fig. 4 Collimated transmittance versus wavelength for phantoms (a) without absorbing centers and (b) with absorbing centers for different thicknesses of phantoms. A and B denote the phantom production series. Vertical line indicates 930-nm wavelength, for which the phantoms were modeled.

3.2 Refractive Index and Dispersion Characteristic

The refractive index (RI) is one of the most important parameters in optics. It is the measure of the phase velocity of light in a medium at a specific wavelength. The mismatch of RIs of the particles and the medium which surrounds them gives rise to light scattering, thus affecting the photon migration in this medium.[27,28,40] It is important to retrieve other optical properties of tissues and consequently, the simulation of tissue phantom parameters. Refractive indices of matrix material (PVCP) and phantoms were measured at 450, 589, 680, 800, 930, and 1100 nm using an Abbe refractometer (DR-M2 1550, Atago, Japan). The values for 930 nm were used as input for the IAD.

Measurements at different wavelengths allow one to plot the dispersion curve (Fig. 5) which can be approximated by the exponential decay:

$$n = 0.437 \cdot e^{(-\lambda/433.689)} + 1.44822, \qquad (6)$$

with a very high correlation coefficient $R^2 = 0.9978$. The dispersion curve is based on RI measurements of the matrix material (PVCP) itself, which were measured with high accuracy up to a fourth decimal place. Since the RI varies slightly between production series when ZnO is added, we used the data
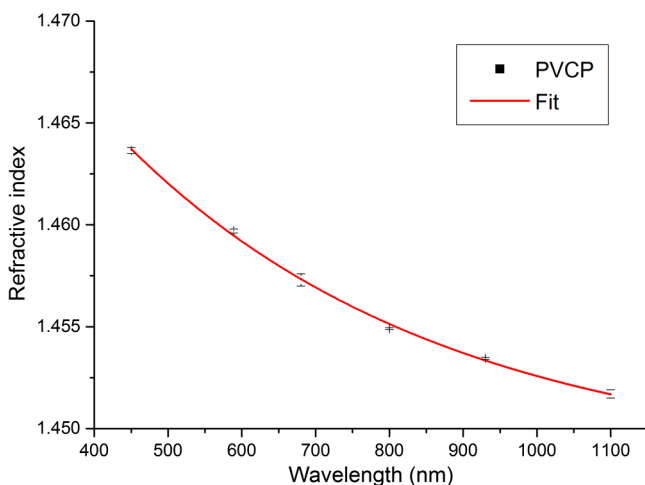
for "clean" (transparent matrix material, without introducing scattering nanoparticles) PVCP, which is a constant. This enables accurate IAD calculations of optical properties at wavelengths different from 930 nm, for which the phantoms' properties were modeled. Thus, if other measurements were performed for different wavelengths, the phantom parameters may be retrieved for the full spectral range with a very high correlation coefficient of measured value, $R^2 = 0.9978$. Examined RI averages 1.4550 ± 0.0005 at 930 nm for all phantoms, as shown in Table 1.

3.3 Geometrical Dimensions and Surface Roughness

We have measured geometrical dimensions of the phantoms, their thickness, and surface roughness. The total attenuation of light by the phantom is determined by its absorption and scattering coefficients and by its thickness. Thickness is crucial for the retrieval of optical properties using the IAD method, since this method is based on an approximation of plane-parallel slabs of finite thickness. Surface roughness introduces errors to the measurements of optical properties due to the thickness

Fig. 5 Dispersion curve of a matrix material (PVCP) in the 450–1100-nm wavelength range.

Table 1 Refractive indices (RIs) of phantoms at 930-nm wavelength.

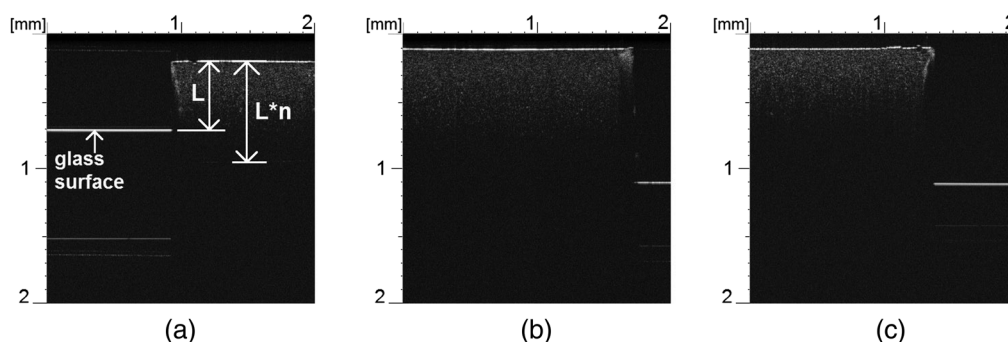| Thickness and sample number	Refractive index	
	Nonabsorbing phantoms	Absorbing phantoms
200 μm A	1.4540	1.4556
200 μm B	1.4546	1.4550
500 μm A	1.4547	1.4550
500 μm B	1.4564	1.4546
1 mm A	1.4550	1.4554
1 mm B	1.4557	1.4549
2 mm A	1.4556	1.4545
2 mm B	1.4553	1.4550

Fig. 6 Optical coherence tomography (OCT) results: (a) measurement of phantom thickness from OCT image, $L * n$ denotes the optical path length as a geometrical path length L between the top of the phantom and the glass surface multiplied by the refractive index n; (b) OCT image of a 1-mm-thick phantom without absorbing centers; and (c) a 1-mm-thick phantoms with absorbing centers. Depth of light penetration is notably greater in the first case.

variation and the results of the following calculations, because a smooth homogeneous surface is assumed by IAD. The magnitude of errors in reconstruction of the phantom optical properties is due to surface roughness and the thickness measurement precision.

A spectral-domain OCT system (Hyperion, Thorlabs, USA) was used for retrieval of the phantom geometrical thickness. OCT depends on the interference of low-coherent light from measurement and sensing arms of the interferometer, thus it is sensitive to the thickness and the RI of a sample.[41–43] For the measurements, the phantoms were placed on a glass slide. The thickness of phantoms was calculated by division of the optical path length from the top of the glass slide through the air and the optical path length through the phantom to the glass slide surface as shown in Fig. 6(a). OCT imaging allows us to also image internal structural inhomogeneities and defects.

The measurements were averaged over an area of about 4 mm^2 in the center of the phantom. Geometrical thickness was determined for all phantoms with accuracy of ± 10 μm. For the 1- and 2-mm-thick phantoms, the relative difference between the assumed thickness (mold inner dimensions) and real thickness was not more than 2%. However, the thinnest phantoms exhibit differences of up to 20%. The internal structure of the phantom is vastly homogenous with negligible particle clusters. Cross-sections of phantoms provide some insight into the surface roughness, which is very limited by the axial resolution of the OCT system (<6 μm in air).

The profiles of the phantom surfaces were measured using a white-light[43,44] profilometer (Bruker, USA) over the area of about 1.7 mm by 2.3 mm. Surface roughness profiles present two extreme cases: the smooth surface of a 2-mm-thick phantom [Figs. 7(a), 7(c), and 7(e)] and a rough surface of a 500-μm-thick phantom [Figs. 7(b), 7(d), and 7(f)]. The latter has a large number of small channels or grooves which were apparently created by the evacuating air bubbles when the mixture has already partially solidified during polymerization.

The surface of a 2-mm-thick phantom is relatively flat with only minimal roughness, approximately $\Delta L = 2$ μm in the X-axis. In the Y-axis, the surface is inclined by <1.4%. The surface roughness of the other phantom in the areas not "affected" by the emergence of the channels is roughly $\Delta L = 5$ μm (not shown). Yet, the channels emergence is unpredictable. They are formed usually around the edges of the phantoms, especially at the bottom of the mold. One of the typical channels is shown, and it is responsible for an absolute error of about $\Delta L = 15$ μm.

We have noticed that if the channels form, they are usually shallow in the thickest phantoms and get deeper for the thinner phantoms. Thus, the error of estimating phantom thickness is even larger when compared with the absolute thickness of the phantom, i.e., the relative error of thickness estimation. The error amounts to 0.1%, 1.5%, 3%, and 20% for the 2-mm-, 1-mm-, 500-μm-, and 200-μm-thick phantoms, respectively. Visible spikes are the result of dust accumulated on the surface and were not taken into account.

4 Calculations of the Optical Properties with Inverse Adding-Doubling

After the measurements of reflectance, transmittance, collimated transmittance, refractive index, and geometrical thickness, the inverse adding-doubling (IAD) method was used to calculate the optical properties. This method relies on the iterative solving of the radiative transport equations with the adding-doubling method and yields the reduced scattering coefficient μ_s' and absorption coefficient μ_a, as well as the anisotropy factor g. The sample is assumed to be an infinite plane-parallel slab with known thickness and RI.

The results of IAD calculations are presented in Figs. 8–11. Figure 8 shows calculated reduced scattering coefficients μ_s' of phantoms with various thicknesses, Fig. 9 shows calculated absorption coefficients μ_a of phantoms with various thicknesses, Fig. 10 shows calculated anisotropy factor g of phantoms with various thicknesses, and Fig. 11 shows calculated scattering coefficient μ_s of phantoms with various thicknesses.

The scattering properties of phantoms were modeled to be similar to those of average human skin in the wavelength range 930 nm. For the 930-nm wavelength, the reduced scattering coefficient (Fig. 8) equals 1.74 ± 0.35 mm^{-1} for nonabsorbing and 1.56 ± 0.14 mm^{-1} for absorbing phantoms. The dependence of this factor on thickness is noticeable but relatively low. For the short wavelengths, significant errors are due to noise in the measured data. The values are wavelength-dependent as predicted by the Mie theory of scattering. Additional absorption does not contribute to the reconstruction of scattering. The estimated values of μ_s' are matched closely to the data of real human skin found in the literature.[11–13]

Calculated results for the absorption coefficient (Fig. 9) show the increase of absorption at 930 nm from 0.05 ± 0.03 to 0.22 ± 0.03 mm^{-1} for all phantoms except the 200-μm-thick. No evident dependence on the wavelength in the full wavelength range was indicated. A slight dependence on the thickness of
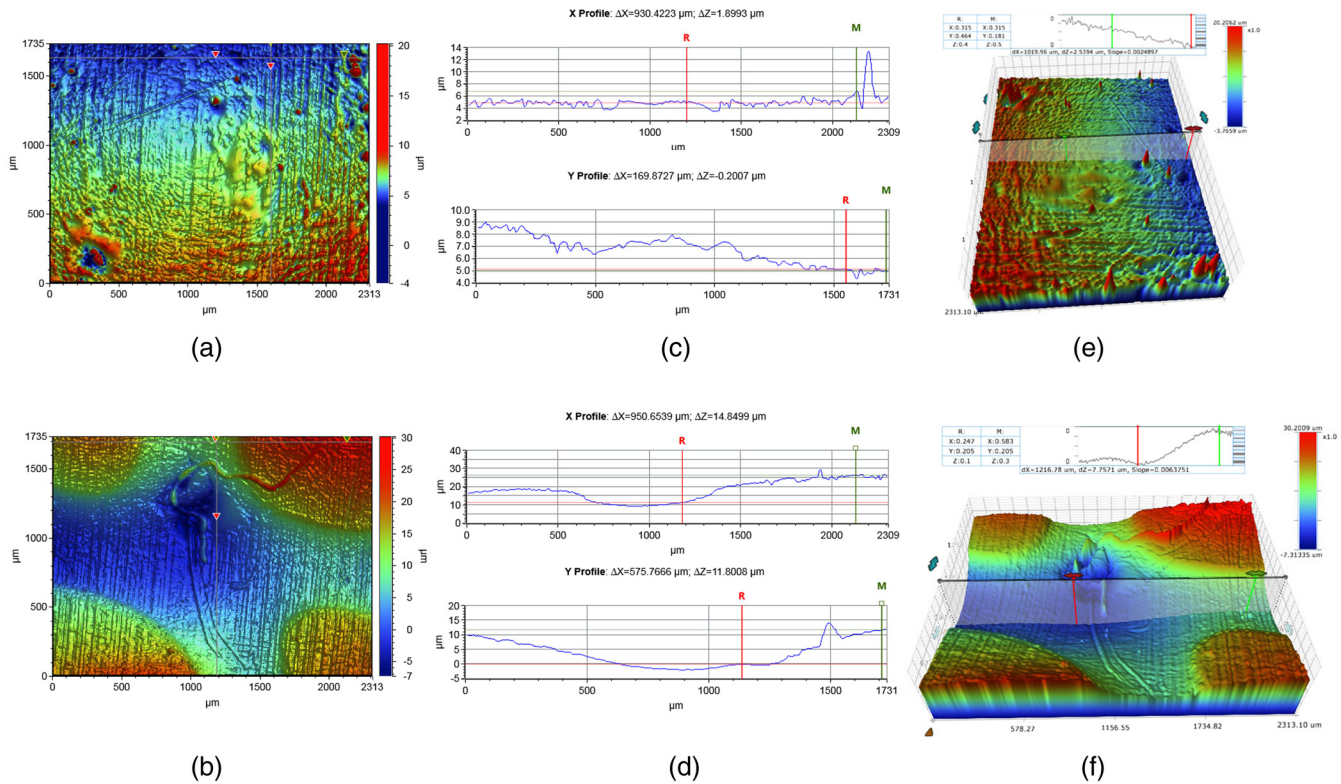
Fig. 7 Surface roughness results for 2-mm-thick (a, c, e) and 500-μm-thick (b, d, f) phantoms. Phantom surface profile maps are presented (a, b) (notice uneven color scales), as well as the X and Y axes profiles (c, d) of the marked cross-sections, and the surface three-dimensional visualizations (e, f).
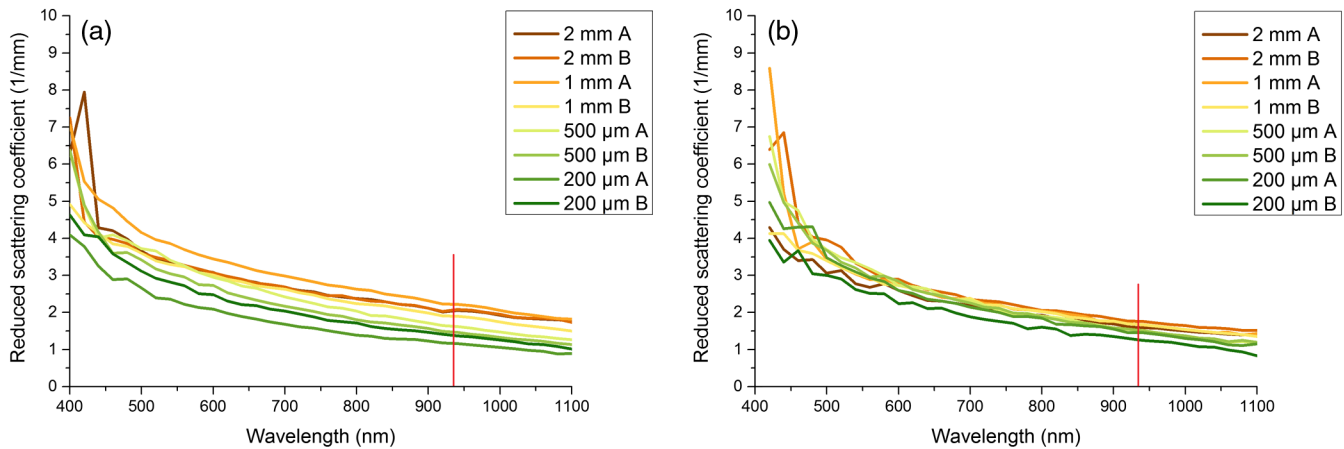

Fig. 8 Calculated reduced scattering coefficients μ_s' of phantoms with various thicknesses: (a) without absorbing substance; and (b) with absorbing substance. Vertical line indicates 930-nm wavelength, for which the phantoms were modeled.

the phantoms is noticeable. The 200-μm-thick phantoms, regardless of the addition of absorption, have significantly overestimated absorption coefficients.

Calculated scattering anisotropy factors (Fig. 10) vary heavily with the phantom thickness. According to the theory,[27,28] the anisotropy factor depends only on the parameters of the scattering particles, such as RI, size distribution, and concentration, and is independent of the thickness of the material. The scattering coefficient (Fig. 11) was calculated as well, according to Eq. (1).

5 Discussion

We have presented a number of optical techniques used to characterize properties of developed tissue phantoms designed for simulating optical properties of human skin at around 930 nm. The OCT imaging is primarily used as a noninvasive diagnostic technique and is often the recipient technique of the phantoms for calibration or research purposes.[45–47] Moreover, it can be used to estimate the phantom geometrical thickness and RI with a precision dependent on its axial resolution. The thicknesses of the produced phantoms were measured with the OCT with an
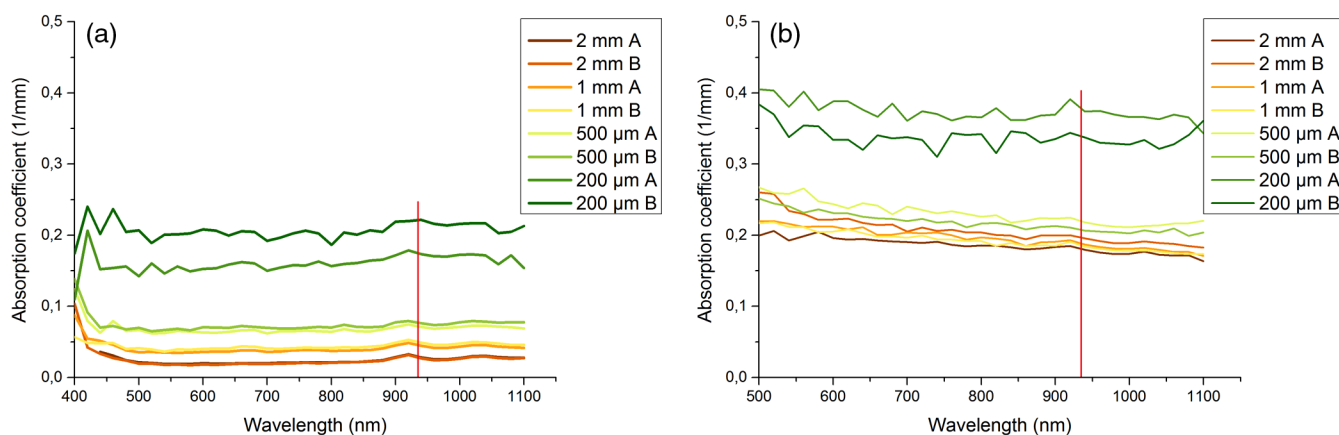
Fig. 9 Calculated absorption coefficients μ_a of phantoms with various thicknesses: (a) without absorbing substance; and (b) with absorbing substance. Wavelength dependence is negligible and thickness dependence is noticeable. The values for 200-μm-thick phantoms are severely overestimated. Vertical line indicates 930-nm wavelength, for which the phantoms were modeled.

accuracy of $\pm 6\ \mu$m (in air). However, some studies show techniques which use OCT for the determination of the microscopic properties.[21,48–50] In-depth scanning allows for investigation of internal inhomogeneities, which are mainly caused by trapped air bubbles and clustering of nanoparticles. No significant inhomogeneities were detected in the produced phantoms. The surface profile of the phantoms was determined with an accuracy <0.01 nm with the use of the white-light profilometer. Production errors such as channels created by evacuating air bubbles during solidification of the phantoms result in large variations in phantom thickness. We have noticed that the magnitude of this effect drops with the increasing thickness of the phantoms. Therefore, the relative error in determination of thickness was greatest for the thinnest phantoms. The maximum relative error ΔL is 0.1%, 1.5%, 3%, and 20% for the 2-mm-, 1-mm-, 500-μm-, and 200-μm-thick phantoms, respectively. The RI was measured for multiple wavelengths, which allowed us to define the dispersion function with $R^2 = 0.9978$

correlation coefficient. The RI at 930 nm was approximately 1.455 ± 0.0005 for all phantoms, which is very similar to that of the real tissues.[28] The spectrophotometric measurements consisted of transmittance, reflectance, and collimated transmittance measurements. Reflectance and transmittance were collected using integrating spheres, while the collimated transmittance was collected with the use of a collimating lens. Measurements were done from 2 s up to 8 s integration time when necessary under low-light conditions. Spectra were obtained from several sites over the central area of the phantoms and then averaged. Since the setup required rearrangement for each type of the measurement, acquiring data from the same spot for all three parameters was impossible and averaging over the middle area of the phantoms had to be done. The reflectance was measured using the comparison method consisting of a total of 2 calibration and 2 sample measurements. The strong dependence on the phantom thickness is evident in transmittance and reflectance measurements. In both of these cases,
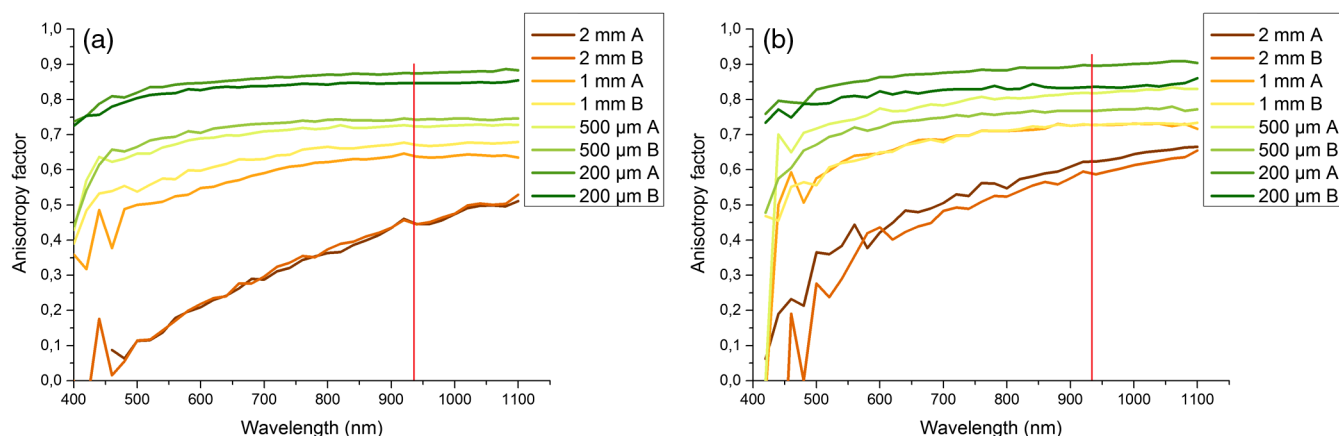

Fig. 10 Calculated anisotropy factor g of phantoms with various thicknesses: (a) without absorbing substance; and (b) with absorbing substance. Results evidently depend on the thickness of the phantoms. The effect of the absorption is greater inaccuracy in the case of low signal levels, such as with thicker phantoms and for shorter wavelengths. Calculation of g factor from collimated transmittance (i.e., scattering coefficient) is very sensitive to thickness and accuracy of extraction of the scattering coefficient. Reduced scattering coefficient is much less sensitive to thickness (Fig. 8), thus g factor is mostly defined by scattering coefficient behavior. Vertical line indicates 930-nm wavelength, for which the phantoms were modeled.
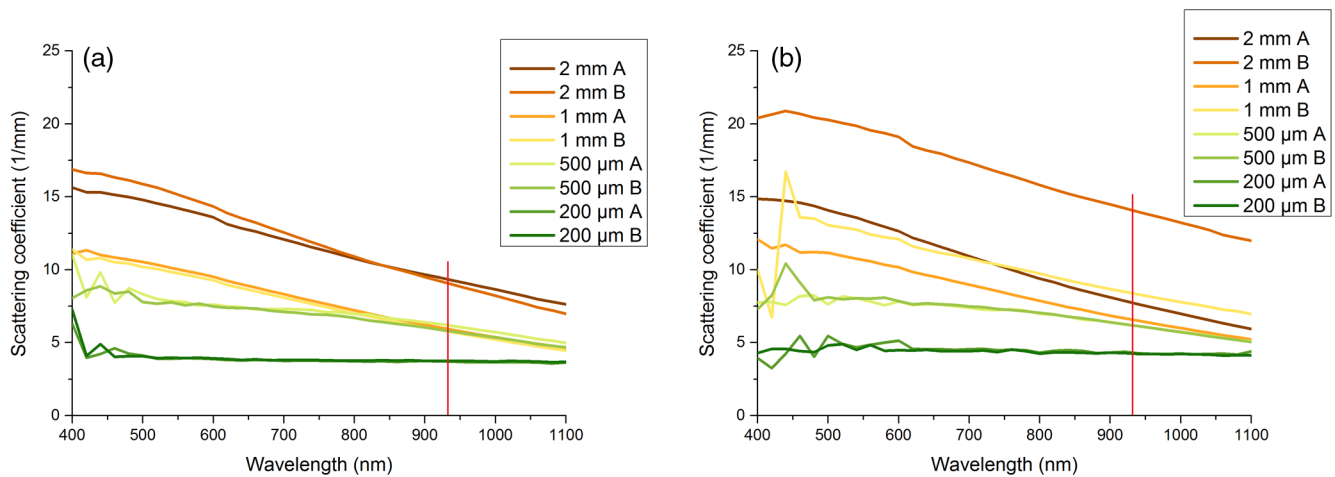
Fig. 11 Calculated scattering coefficient μ_s of phantoms with various thicknesses: (a) without absorbing substance; and (b) with absorbing substance. Calculated scattering is dependent on phantom thickness. The introduction of absorbing agent does not interfere strongly with the scattering properties. Therefore, matching each parameter independently is possible with the used scattering and absorbing substances. Vertical line indicates 930-nm wavelength, for which the phantoms were modeled.

the introduction of absorption leads to a decrease of the measured values, which means that the observations are in agreement with the theoretical assumptions. The amount of light in collimated transmittance measurements is extremely low and, therefore, the most susceptible to noise. The results vary greatly with the phantoms' thicknesses, even in spot-to-spot measurements over the same phantom. The IAD method was used to calculate the μ_s', μ_a, and g factor. The averaged (over all samples) reduced scattering coefficient for 930 nm equals 1.74 ± 0.35 and 1.57 ± 0.14 mm^{-1} for nonabsorbing and absorbing phantoms, respectively. This values lie in close proximity with the values found in the literature for the reduced scattering coefficient of human skin.[11–14] This proves the correctness of theoretical assumptions and the proper fabrication of the phantoms for the specified goal of mimicking the optical properties of human skin at 930 nm. The absorption coefficient increased from 0.05 ± 0.03 to 0.22 ± 0.03 mm^{-1} for all phantoms except the 200-μm-thick. These values are in agreement with the average absorption coefficients found in the literature data.[11–14] The absorption coefficient for 200-μm thick phantoms was overestimated by 0.2 mm^{-1}. This must be mainly due to the small size of the phantom, which causes light to escape from the edges, thus breaking the IAD assumption which was found to cause overestimations of the absorption coefficient.[30,31] The anisotropy factor results depend greatly on phantom thickness. Since the anisotropy theoretically depends only on the particle parameters and their amount and size distribution in a medium,[27,28] it should be constant regardless of the sample thickness. This leads to the conclusion that the calculated g factors are based on erroneous measurements. Possible sources of this error are: (1) surface roughness (thickness difference) of the phantom surface between the measured spots; (2) uncertainty in measurements of thickness; (3) low signal intensity on the detector when measuring $T_c(\lambda)$ so that the noise introduces a large amount of error; and (4) detection of partially scattered light in unscattered transmission measurement, which probably had the most influence on incorrect g estimation. A quite reasonable experimental value for the g factor of 0.8 was obtained for thin samples due to less influence of multiple scattered light on collimated transmittance measurements in that case and a weak

sensitivity of the reduced scattering coefficient to sample thickness. The consequence of the latter has been reported as causing the estimation of optical properties dependent on the thickness of the measured material.[30,31] This was also evident in our study, however, the μ_s' and μ_a dependences on thickness were mostly acceptable as an expected inaccuracy of estimation caused by the limited accuracy of the measurements.

Acknowledgments

References

1. V. O. Korhonen et al., "Light propagation in NIR spectroscopy of the human brain," *IEEE J. Sel. Top. Quantum Electron.* **20**, 1–10 (2014).
2. T. Myllylä et al., "Optical sensing of a pulsating liquid in a brain-mimicking phantom," *Proc. SPIE* **8799**, 87990X (2013).
3. E. Alarousu et al., "Noninvasive glucose sensing in scattering media using OCT, PAS, and TOF techniques," *Proc. SPIE* **5474**, 33–41 (2004).
4. M. Jedrzejewska-Szczerska et al., "Fiber-optic temperature sensor using low-coherence interferometry," *Eur. Phys. J. Spec. Top.* **154**(1), 107–111 (2008).
5. A. E. Cerussi et al., "Tissue phantoms in multicenter clinical trials for diffuse optical technologies," *Biomed. Opt. Express* **3**, 966–971 (2012).
6. H. S. S. Sorvoja et al., "Non-invasive, MRI-compatible fibreoptic device for functional near-IR reflectometry of human brain," *Quantum Electron.* **40**, 1067 (2010).
7. J. Hwang, J. C. Ramella-Roman, and R. Nordstrom, "Introduction: feature issue on phantoms for the performance evaluation and validation of optical medical imaging devices," *Biomed. Opt. Express* **3**, 1399–1403 (2012).
8. M. L. Clarke et al., "Designing microarray phantoms for hyperspectral imaging validation," *Biomed. Opt. Express* **3**, 1291–1299 (2012).

9. D. V. Samarov et al., "Algorithm validation using multicolor phantoms," *Biomed. Opt. Express* **3**, 1300–1311 (2012).
10. A. Mazikowski, R. Hypszer, and M. Jedrzejewska-Szczerska, "Modeling of non-contact temperature measurement system using multiwavelength pyrometry," *Proc. SPIE* **4516**, 120–124 (2001).
11. W.-F. Cheong, S. A. Prahl, and A. J. Welch, "A review of the optical properties of biological tissues," *IEEE J. Quantum Electron.* **26**, 2166–2185 (1990).
12. A. N. Bashkatov, E. A. Genina, and V. V. Tuchin, "Optical properties of skin, subcutaneous, and muscle tissues: a review," *J. Innovative Opt. Health Sci.* **04**, 9–38 (2011).
13. T. Lister, P. A. Wright, and P. H. Chappell, "Optical properties of human skin," *J. Biomed. Opt.* **17**, 090901 (2012).
14. S. L. Jacques, "Optical properties of biological tissues: a review," *Phys. Med. Biol.* **58**, R37–R61 (2013).
15. M. S. Wróbel et al., "Multi-layered tissue head phantoms for noninvasive optical diagnostics," *J. Innovative Opt. Health Sci.* **8**, 1541005 (2015).
16. B. W. Pogue and M. S. Patterson, "Review of tissue simulating phantoms for optical spectroscopy, imaging and dosimetry," *J. Biomed. Opt.* **11**, 041102 (2006).
17. R. J. Nordstrom, "Phantoms as standards in optical measurements," *Proc. SPIE* **7906**, 79060H (2011).
18. G. Lamouche et al., "Review of tissue simulating phantoms with controllable optical, mechanical and structural properties for use in optical coherence tomography," *Biomed. Opt. Express* **3**, 1381–1398 (2012).
19. R. B. Saager et al., "Multilayer silicone phantoms for the evaluation of quantitative optical techniques in skin imaging," *Proc. SPIE* **7567**, 756706 (2010).
20. M. Jędrzejewska-Szczerska et al., "Investigation of photothermolysis therapy of human skin diseases using optical phantoms," *Proc. SPIE* **9447**, 944715 (2015).
21. A. Agrawal et al., "Characterizing the point spread function of retinal OCT devices with a model eye-based phantom," *Biomed. Opt. Express* **3**, 1116–1126 (2012).
22. R. C. Chang et al., "Fabrication and characterization of a multilayered optical tissue model with embedded scattering microspheres in polymeric materials," *Biomed. Opt. Express* **3**, 1326–1339 (2012).
23. J. Fu et al., "A simple method of obtaining the reduced scattering coefficients of tissue-simulating phantoms," *J. Innovative Opt. Health Sci.* **03**, 53 (2010).
24. S. L. Jacques, B. Wang, and R. Samatham, "Reflectance confocal microscopy of optical phantoms," *Biomed. Opt. Express* **3**, 1162–1172 (2012).
25. H. Kang et al., "Multimodal optical studies of single and clustered colloidal quantum dots for the long-term optical property evaluation of quantum dot-based molecular imaging phantoms," *Biomed. Opt. Express* **3**, 1312–1325 (2012).
26. S. C. Kanick et al., "Scattering phase function spectrum makes reflectance spectrum measured from Intralipid phantoms and tissue sensitive to the device detection geometry," *Biomed. Opt. Express* **3**, 1086–1100 (2012).
27. V. V. Tuchin, "Light scattering study of tissues," *Phys.-Usp.* **40**, 495 (1997).
28. V. V. Tuchin, *Tissue Optics: Light Scattering Methods and Instruments for Medical Diagnosis*, SPIE Press, Bellingham, Washington (2007).
29. B. C. Wilson, M. S. Patterson, and S. T. Flock, "Indirect versus direct techniques for the measurement of the optical properties of tissues," *Photochem. Photobiol.* **46**, 601–608 (1987).
30. J. W. Pickering et al., "Double-integrating-sphere system for measuring the optical properties of tissue," *Appl. Opt.* **32**, 399–410 (1993).
31. S. A. Prahl, M. J. van Gemert, and A. J. Welch, "Determining the optical properties of turbid media by using the adding-doubling method," *Appl. Opt.* **32**, 559–568 (1993).
32. J. R. Mourant et al., "Predictions and measurements of scattering and absorption over broad wavelength ranges in tissue phantoms," *Appl. Opt.* **36**, 949–957 (1997).
33. G. C. Beck et al., "Design and characterization of a tissue phantom system for optical diagnostics," *Lasers Med. Sci.* **13**, 160–171 (1998).
34. T. Moffitt, Y.-C. Chen, and S. A. Prahl, "Preparation and characterization of polyurethane optical phantoms," *J. Biomed. Opt.* **11**, 041103 (2006).
35. S. S. Kumar et al., "Synthesis, characterization and optical properties of zinc oxide nanoparticles," *Int. Nano Lett.* **3**, 1–6 (2013).
36. Q. Wang, K. Shastri, and T. J. Pfefer, "Experimental and theoretical evaluation of a fiber-optic approach for optical property measurement in layered epithelial tissue," *Appl. Opt.* **49**, 5309–5320 (2010).
37. R. X. Xu et al., "Dual-mode imaging of cutaneous tissue oxygenation and vascular function," *J. Visualized Exp.* **46**, 2095 (2010).
38. L. Luu et al., "Microfluidics based phantoms of superficial vascular network," *Biomed. Opt. Express* **3**, 1350–1364 (2012).
39. T. T. Nguyen et al., "Three-dimensional phantoms for curvature correction in spatial frequency domain imaging," *Biomed. Opt. Express* **3**, 1200–1214 (2012).
40. H. C. van de Hulst, *Light Scattering by Small Particles*, Dover Publications, New York (1981).
41. M. Jedrzejewska-Szczerska, B. B. Kosmowski, and R. Hypszer, "Shaping of coherence function of sources used in low-coherent measurement techniques," *J. Phys. IV* **137**, 103–106 (2006).
42. M. Jedrzejewska-Szczerska, "Shaping coherence function of sources used in low-coherent measurement techniques," *Eur. Phys. J.-Spec. Top.* **144**, 203–208 (2007).
43. J. Pluciński et al., "Optical low-coherence interferometry for selected technical applications," *Bull. Pol. Acad. Sci. Tech. Sci.* **56**(2), 155–172 (2008).
44. M. Jędrzejewska-Szczerska et al., "Theoretical and experimental investigation of low-noise optoelectronic system configurations for low-coherent optical signal detection," *J. Phys. IV France* **137**, 107–110 (2006).
45. A. V. Bykov et al., "Skin phantoms with realistic vessel structure for OCT measurements," *Proc. SPIE* **7376**, 73760F (2010).
46. A. V. Bykov et al., "Multilayer tissue phantoms with embedded capillary system for OCT and DOCT imaging," *Proc. SPIE* **8091**, 80911R (2011).
47. J. Baxi et al., "Retina-simulating phantom for optical coherence tomography," *J. Biomed. Opt.* **19**, 021106 (2014).
48. D. Faber et al., "Quantitative measurement of attenuation coefficients of weakly scattering media using optical coherence tomography," *Opt. Express* **12**, 4353–4365 (2004).
49. Y. Yang et al., "Optical scattering coefficient estimated by optical coherence tomography correlates with collagen content in ovarian tissue," *J. Biomed. Opt.* **16**, 090504 (2011).
50. X. Xu, J. Lin, and F. Fu, "Optical coherence tomography to investigate optical properties of blood during coagulation," *J. Biomed. Opt.* **16**(9), 096002 (2011).

Maciej S. Wróbel received his BSc and MSc degrees in electronics and telecommunication, with a specialty of optoelectronics, from Gdańsk University of Technology in 2012 and 2013, respectively. He is currently a PhD student at the same university. His main research area is biophotonics and he focuses on spectroscopic methods of biotissue analysis, tissue-mimicking phantoms for noninvasive optical sensing, signal processing, and fiber-optic sensors.

Alexey P. Popov graduated from the Physics Department of Moscow State University (Russia) in 2003 and received his PhD in 2006 from the same university and his DSc(Tech) degree from the University of Oulu (Finland) in 2008. He is currently a docent in the University of Oulu. His scientific interests are in the area of nanobiophotonics, nanoparticle-light-tissue-cell interaction, including biotissue-mimicking phantoms, deep-tissue imaging using up-conversion nanoparticles, enhancement of skin UV protection by sunscreens, and cell optoporation by plasmonic nanostructures.

Alexander V. Bykov is a postdoctoral researcher in the University of Oulu. He received his MSc diploma in physics at the M.V. Lomonosov Moscow State University in 2005 and his PhD in 2008 from the same university. In 2010 he received a DSc(Tech) degree from the University of Oulu. His scientific interests are in the area of biophotonics, noninvasive optical diagnostics, theory of light propagation in scattering media including biotissues, and numerical simulation of light transport.

Matti Kinnunen received his MSc (Tech) and DSc (Tech) degrees in electrical engineering from the University of Oulu, Oulu, Finland, in 2002 and 2006, respectively. He is currently working as a senior research fellow at the University of Oulu. His research interests

include light-matter interactions in tissues and at the single cell level, sensors and measurement techniques, as well as optical noninvasive measurement techniques for biomedical applications.

Malgorzata Jędrzejewska-Szczerska received her PhD degree with honors in electronics from the Gdańsk University of Technology in 2008. Currently she is an assistant professor in the Department of Metrology and Optoelectronics. Her main research area is biophotonics, and she focuses on use of low-coherence interferometry, fiber-optic technology, and application of optical measurements in biomedicine.

Valery V. Tuchin is a professor and chairman of Optics and Biophotonics at Saratov State University, Russia. He is also the head of laboratory, Institute of Precision Mechanics and Control, RAS. His research interests include biophotonics, tissue optics, laser medicine, tissue optical clearing, and nanobiophotonics. He is a member of SPIE, OSA, and IEEE, and a fellow of SPIE and has been awarded honored science worker of the Russia, SPIE educator award, and FiDiPro (Finland).